The Cryosphere Discuss., 6, 673–714, 2012
www.the-cryosphere-discuss.net/6/673/2012/
doi:10.5194/tcd-6-673-2012

The Cryosphere Discussions

Uncertainty in future solid ice discharge from Antarctica

R. Winkelmann[1,2], A. Levermann[1,2], K. Frieler[1], and M. A. Martin[1,2]

[1]Earth System Analysis, Potsdam Institute for Climate Impact Research, Potsdam, Germany
[2]Institute of Physics, Potsdam University, Potsdam, Germany

Received: 23 January 2012 – Accepted: 6 February 2012 – Published: 14 February 2012

Correspondence to: R. Winkelmann (ricarda.winkelmann@pik-potsdam.de)

Published by Copernicus Publications on behalf of the European Geosciences Union.

Abstract

Future solid ice discharge from Antarctica under climate scenarios based on the Extended Concentration Pathways is investigated with the Potsdam Parallel Ice Sheet Model (PISM-PIK), a shallow model with a consistent representation of the ice flow in sheet, shelves and the transition zone. Both the uncertainty in the climate forcing as well as the intra-model uncertainty are combined into a probability distribution for solid ice discharge from Antarctica until the year 2500 under the ECP scenarios: All simulations are performed for a 81-member perturbed-physics ensemble and the likely ranges of surface and ocean warming under the emission pathways derived from the results of 20 CMIP3-AOGCMS. The effects of surface warming, ocean warming and increased precipitation on solid ice discharge are separately considered. We find that solid ice discharge caused by enhanced sub-shelf melting exceeds that caused by surface warming. Increasing precipitation leads to a change from net sea-level rise to sea-level drop. Our results suggest that the history of the ice-sheet plays an important role with respect to projections of solid ice discharge. Although all climate-change-forced simulations begin with the year 1850, the ice discharge around 2000 is significantly smaller than observed. Observed changes in ice discharge are reached around 2077 under the ECP-8.5 scenario. During the subsequent century, ice discharge reaches up to 0.24 m.

1 Introduction

The unknown dynamic contribution of the Antarctic Ice Sheet imposes a large uncertainty on future global sea-level projections (Meehl et al., 2007). Observations suggest that Antarctica is currently losing mass (Rignot et al., 2011), but it is unclear whether this trend will continue or whether an increase in accumulation as expected in a warming atmosphere (Uotila et al., 2007) will lead to future mass gain. This depends strongly on the different dynamical processes controlling solid ice discharge, including

TCD
6, 673–714, 2012

the buttressing effect of ice shelves, ice softening through warming and changes in driving stress near the grounding line. Numerical ice-sheet models provide a way of incorporating these processes and their interaction in future sea-level projections.

Prior assessments with process-based models reveal a broad range of possible responses of the Antarctic Ice Sheet to future warming, from negative to positive contributions to global sea-level rise (e.g., Huybrechts et al., 2004; Vizcaino et al., 2008, 2010; Huybrechts et al., 2011). They stress the importance of including shelf dynamics and the transition between the different flow regimes in sheet and shelves with the potential for rapid dynamic changes. A large uncertainty remains with respect to the choice of model input parameters which have a strong influence on the processes governing solid ice discharge (Applegate et al., 2011; Martin et al., 2012).

Here, we present projections from a perturbed-physics ensemble of the Antarctic Ice Sheet for climate scenarios based on the Extended Concentration Pathways (ECP, Meinshausen et al., 2011b).

The simulations are conducted with the Potsdam Parallel Ice Sheet Model (PISM-PIK, Winkelmann et al., 2011), a continental-scale ice-sheet model especially suited for simulations of Antarctica (Martin et al., 2011), with a horizontal resolution of approximately 18 km. The modelling approach is based on the Shallow Ice Approximation (SIA) and the Shallow Shelf Approximation (SSA) which make use of the fact that ice thickness is small compared to relevant horizontal scales. The respective equations are solved simultaneously on the whole ice body. The ice velocity is obtained by superposing the two solutions from SIA and SSA, allowing for a consistent treatment of sheet, shelves and the transition zone, as illustrated in Fig. 1. PISM-PIK includes a sub-grid parameterization of ice-front motion (Albrecht et al., 2011) and a dynamic calving law (Levermann et al., 2011). The position of the grounding line evolves freely according to the flotation criterion. Aiming at a more realistic representation of the basal melt patterns which differ significantly among the ice shelves attached to the Antarctic Ice Sheet, basal melting and refreezing are computed based on the ocean box-model introduced by Olbers & Hellmer (2010), see Sect. 3.2.

TCD
6, 673–714, 2012

In the following, we give an overview of the ensemble of initial states, which were selected to resemble the present geometry of the Antarctic Ice Sheet but differ in their sensitivity to climate forcing (Sect. 2). The derivation of the forcing scenarios underlying our projections is outlined in Sect. 3.1, followed by a description of how sub-shelf melt rates (Sect. 3.2) are computed. This module is new within PISM-PIK compared to the description in Winkelmann et al. (2011). In Sect. 3.3 we specify how we derive an uncertainty distribution for the dynamic ice loss from Antarctica, comprising both the uncertainty in the forcing as well as the intra-model uncertainty. The results from the perturbed-physics ensemble under the ECP scenarios are discussed in Sect. 4. We separate the different effects of a changing climate on the Antarctic Ice Sheet by performing three sets of experiments: First, we only change the surface temperature according to the ECP scenarios (Sect. 4.1). Second, we include the effect of a warming ocean and the resulting increase in sub-shelf melting (Sect. 4.2). Third, we additionally allow for changes in precipitation on Antarctica through atmospheric warming (Sect. 4.3). A brief discussion of the time-delay found between forcing and ice response (Sect. 4.4) is followed by the summary and conclusions in Sect. 5.

2 The perturbed-physics ensemble

A number of physical parameters in ice sheet models such as PISM-PIK are highly uncertain. Most important with regards to the transport across the grounding line relevant for sea-level rise are the two enhancement factors, E_{SIA} and E_{SSA}, and the pore-water fraction F_{p} which controls the basal friction of grounded ice, especially important in the transition zone. The enhancement factors $E_{\mathrm{SIA}} > 1$ and $E_{\mathrm{SSA}} < 1$ (see equations (4) and (10) in Winkelmann et al. (2011)), are used within the Shallow Ice Approximation and the Shallow Shelf Approximation, respectively, in order to include differences in the rheology of ice which cannot be modelled explicitly in large-scale ice-sheet models such as PISM-PIK. The pore-water fraction $F_{\mathrm{p}} < 1$ (see equation (13) in Winkelmann et al. (2011)) regulates the yield stress at which the bed fails and is

TCD
6, 673–714, 2012

crucial for the ice velocities in streams and thereby the transport across the grounding line. For these parameters, Martin et al. (2012) perform a sensitivity study of the dynamic ice loss of Antarctica under the SeaRISE experiments (SeaRISE, 2011; Bindschadler, n.d.) with the Parallel Ice Sheet Model (PISM) (PISM-authors, n.d.), showing that the response of the ice-sheet to external forcings such as idealized enhanced melting and sliding as well as changes in surface temperature and accumulation is highly dependent on the choice of parameters.

In order to quantify the uncertainty of sea-level projections resulting from the unknown physics captured in these parameters, E_{SIA}, E_{SSA} and F_{p} are varied as shown in Table 1. The parameter spread for E_{SIA} corresponds to the range obtained by Ma et al. (2010) from simulations with a full-Stokes anisotropic marine ice-sheet flowline model. E_{SSA} and F_{p} are sampled to cover a broad range of potential ice dynamics.

For each parameter combination, the model is run into equilibrium starting from present-day boundary conditions (Le Brocq et al., 2010). The spin-up process for all initial states is analogous to the one described in Martin et al. (2011). The resulting equilibrium states of the Antarctic Ice Sheet vary in properties such as ice volume, thickness, velocity patterns and grounding line position.

Aiming at maintaining a large range of representations of the ice dynamics, we exclude only those of all possible parameter combinations for which the geometry of the ice sheet in the associated equilibrium state deviates strongly from present-day observations. In particular, we do not allow the sea-level relevant volume of the West Antarctic Ice Sheet to deviate by more than 10 % from the observed volume. The deviation of the grounding line position from the presently observed position is characterized for each shelf by the anomaly in ice area which may not exceed 10 % of the observed area of the attached ice shelf.

The remaining parameter combinations are marked in green in Fig. 2. The enhancement factor of the SIA, governing the viscosity of grounded ice, has the largest influence on the ice volume. The grounding line position is predominantly determined by E_{SSA} and F_{p}. For both criteria to be met, the flux across the grounding line needs to be

TCD
6, 673–714, 2012

limited, resulting in a corridor of possible combinations of E_{SSA} and F_p which excludes cases of strong basal friction in combination with low viscosity or weak basal resistence in combination with high viscosity in streams which lead to a significant advance or retreat of the grounding line within the equilibrium simulation.

The 81 remaining realizations of the Antarctic Ice Sheet serve as initial states for future projections under the climate scenarios described in Sect. 3.

3 Climate forcing

3.1 Temperature pathways based on the Extended Concentration Pathways

The climate scenarios underlying the projections of solid ice discharge from Antarctica are based on the Representative Concentration Pathways (van Vuuren et al., 2011), a set of four pathways spanning a wide range of possible future greenhouse gas emissions, and their extensions, the Extended Concentration Pathways (ECPs, Meinshausen et al., 2011b). The lower and upper bounds are given by the ECP-2.6 and the ECP-8.5 scenario, respectively. The ECP-2.6 scenario is a peak-and-decline scenario which reaches the maximum of greenhouse gas concentrations in the 21st century whereas greenhouse gas concentrations continue to rise until 2250 in the ECP-8.5 scenario.

For each ECP, an uncertainty distribution of global mean temperature anomalies was generated by means of the reduced-complexity coupled carbon-cycle climate model MAGICC 6.0 (Meinshausen et al., 2011a) by historical constraining (Meinshausen et al., 2009). For the resulting global mean temperature changes, see for example Schewe et al. (2011).

It is well established that global mean temperature changes and regional temperature changes exhibit a strong correlation in many AOGCMs (e.g., Giorgi, 2008; Frieler et al., 2011). Figure 3 shows ten-year averages of the annual surface temperature changes (compared to the associated pre-industrial or present-day control runs) for 20

TCD
6, 673–714, 2012

CMIP3-AOGCMs (Meehl et al., 2007). Different colors refer to different climate scenarios. For all AOGCMs, the regional and global temperature changes show a close linear relation with a mean scaling coefficient of approximately 1.09. The spread of the AOGCM-specific scaling coefficients together with the uncertainty distribution found for global mean temperature change are transferred into uncertainty ranges for future temperature changes over Antarctica as described in Frieler et al. (2011). For the projections of solid ice discharge from Antarctica, the resulting surface temperature pathways (Fig. 4) are applied to the field of surface temperatures computed in PISM-PIK as a function of latitude and surface elevation (see Martin et al. (2011), equation (1)).

We have also found a close-to-linear relation between global mean temperature changes and ocean temperature changes in the vicinity of individual Antarctic ice shelves. The correlation is highest when a time-lag is applied to the ocean-temperature changes. For each CMIP3-AOGCM we selected the time-lag providing the highest correlation. For the Ross, Filchner-Ronne, Amery and Pine Island regions, we then chose the model with the highest scaling coefficient, shown in Fig. 5. The projections of solid ice discharge including ocean warming (Sect. 4.2 and 4.3) therefore yield an upper estimate of the effect. Since the lowest scaling coefficients are approximately zero, the projections neglecting ocean warming (Sect. 4.1) can be understood as the lower bound. In the simulations with PISM-PIK, the ocean temperature anomalies are applied with the respective time-lag (see Table 2). However, we will show in Sect. 4.2 that this time-lag has only little impact on the dynamic ice loss until 2500.

3.2 Sub-shelf melting

Strong variability in temperature and salinity observed underneath the Antarctic ice shelves cause different melting and refreezing rates covering several orders of magnitude, with the highest melt rates observed underneath the ice shelf attached to Pine Island Glacier in excess of 40 m yr^{-1} near the grounding line (Rignot & Jacobs, 2002; Payne et al., 2007).

TCD
6, 673–714, 2012

In order to capture this wide spread of melting rates, we use an approach based on the two-dimensional ocean box model by Olbers & Hellmer (2010) which simulates the main overturning circulation in an ice shelf cavern based on six ocean boxes. Two of these boxes interact with the shelf ice (see Fig. 1): Ocean box B_g is close to the grounding line and covers about one third of the ice shelf base while the remaining two thirds up to the shelf front are covered by box B_s. In PISM-PIK, we find the boxes B_g and B_s recursively for each ice shelf. We then compute the basal melt rate of each ice grid-cell bordering one of these two ocean boxes as a function of the temperature and salinity in box B_0 at the cavern entrance. Olbers & Hellmer (2010, Appendix) give the equilibrium solution for the basal melt rate of the ice adjoining B_g for a fixed shelf geometry, accounting for advective but neglecting diffusive processes. In PISM-PIK, we compute the basal melt rate in B_s accordingly from the properties of B_0 and the previously derived solution for B_g. Due to the incorporation in PISM-PIK, ice thickness changes are directly taken into account and the resulting basal melt patterns depend both on the three-dimensional shelf geometry and the ocean boundary conditions.

We initialize the ocean box model with observed salinities and temperatures near the Ross (Jacobs & Giulivi, 1998), Filchner-Ronne (Grosfeld et al., 2001; Nicholls et al., 2003), Amery (Wong et al., 1998) and Pine Island Ice Shelves (Hellmer et al., 1998) from which we substracted the anomalies (generated as described in Sect. 3.1) of the observed years to 1850, the first year of the forced simulations (see Table 3). Figure 6 shows observed basal melt rates in comparison to the modeled basal melt rates in B_g and B_s for the year 2000 as well as the modeled melt rates for the years 2100, 2300 and 2500 of the ECP-4.5 scenario. (Note that the basal melt rate underneath Pine Island Shelf is scaled in this plot by a factor of 0.02.) For the Ross, Filchner-Ronne and Amery Ice Shelves, the observed values lie within the modeled range for the year 2000. The basal melt rate underneath Pine Island Shelf is slightly underestimated but the large difference in magnitude compared to the other shelves is well captured.

TCD
6, 673–714, 2012

3.3 Combining ice-ocean- and climate-uncertainty

The projections of solid ice discharge from Antarctica presented in Sect. 4 are subject to two sources of uncertainty, originating (1) from the spread in the regional projections of air temperature and (2) from the unknown ice parameters used in PISM-PIK. In order to capture both uncertainties, we force each of the 81 initial states with the temperature anomalies corresponding to the 33rd, 50th and 66th percentiles of the full range of regional temperature projections for a given ECP scenario. From the results of these simulations, the uncertainty range in solid ice discharge is computed as follows: For each year of an ECP scenario we randomly pick a parameter combination from the perturbed-physics ensemble, providing the projected ice loss for the temperature pathways associated with the 33rd, 50th and 66th percentiles. Assuming an underlying log-normal distribution for the ice loss, we can compute the respective location and scaling parameters, μ and σ, of the probability density function

$$p(x,\mu,\sigma) = \frac{1}{x\sigma\sqrt{2\pi}} e^{-\frac{(\ln x-\mu)^2}{2\sigma^2}}, \quad x>0 \tag{1}$$

which allows for the possibility of a skewed distribution of the variable x. We then draw one realization from this log-normal distribution. This procedure is repeated 10 000 times for each year of the simulation, yielding a sample of the full uncertainty distribution comprising both sources of uncertainty. From the full distribution, we compute the likely and very likely ranges of ice loss, defined by the 33rd and 66th percentiles and the 5th and 95th percentiles, respectively.

4 Future ice loss under the ECP scenarios

As detailed in Sect. 3.3, we force each of the 81 initial states of the Antarctic Ice Sheet with a low, medium and high temperature pathway for the four ECP scenarios (corresponding to the 33rd, 50th and 66th percentiles of the respective temperature

TCD
6, 673–714, 2012

projections). The following results are thus based on a set of 972 simulations from which the results of the respective control runs are substracted. Climate forcing is applied for the years 1850 to 2500. We have performed the whole set of simulations for surface warming only (Sect. 4.1), surface and ocean warming (Sect. 4.2) and surface and ocean warming including precipitation increase (Sect. 4.3).

4.1 Surface warming

In the first set of experiments we study the ice loss from Antarctica solely caused by surface warming: Figure 7 shows the vertically-averaged ice temperature change for the years 2100 and 2500 of the ECP-8.5 scenario. While surface temperature anomalies are applied uniformly to the whole ice-sheet, the temperature changes at depth are dependent on the local ice properties governing the heat transfer.

Warming of the ice makes it generally softer which increases its velocity and thereby the overall ice flux, especially near the ice-sheet margins as shown exemplarily in Fig. 8 for the same scenario and ice parameters as Fig. 7.

For the ECP-8.5 scenario, the evolution of ice loss through surface warming until year 2500 is shown in Fig. 9a. For the whole perturbed-physics ensemble, the bulk of sea-level rise happens after 2100 – by the end of the 21st century, the maximal sea-level response to surface warming is 0.03 m, thereafter significantly increasing up to 0.58 m in 2500. This delay between sea-level response and temperature forcing is robust for all parameter combinations and will be further discussed in Sect. 4.4. However, the magnitude of the sea-level response depends on the parameter combination. In Fig. 9a, the color is picked accordingly: Sea-level curves marked in red correspond to initial states with high F_p and high E_{SSA}, i.e. ice streams of low viscosity subject to weak basal resistence. These states of the Antarctic Ice Sheet exhibit the strongest dynamic response to surface warming.

Although E_{SIA} is crucial for the ice volume of the initial state, there is no clear dependence on this parameter within the time-scale of the scenarios (see Fig. 9b).

TCD
6, 673–714, 2012

4.2 Ocean and surface warming

Additional ocean warming indirectly affects the flux across the grounding line: Due to enhanced sub-shelf melting, the surface elevation of an ice shelf is lowered, thereby increasing the driving stress across the grounding line. This effect is negligible within the 21st century – compared to the case of surface warming only, it makes a maximal difference of 6 % in total ice loss. However, ocean warming has a large impact on total ice loss thereafter, approximately doubling sea-level rise until 2500. Fig. 9a shows the sea-level response to combined surface and ocean warming for the upper ECP-8.5 scenario compared to that for surface warming only discussed in Sect. 4.1. The shading is picked accordingly, i.e. dark gray is assigned to those ensemble members with the highest F_p and E_{SSA}. The model spread for this one scenario amounts to about 54 % of the mean sea-level response, stressing the importance of including parametric uncertainty in sea-level projections.

In general, sea-level response and initial volume of the West Antarctic Ice Sheet, both determined by the ice characteristics captured in the physical parameters, are anti-correlated. Figure 10 shows the ice loss for each century of the strongest warming scenario as a function of the ice volume above sea-level of the West Antarctic Ice Sheet. Since the projections start from equilibrium states which are all subject to the same precipitation field (precipitation is only changed within the scenarios given in Sect. 4.3), the ice flux balancing it must necessarily be the same also. Yet, this balance flux is attained by different representations of the ice-physics which give rise to different velocity and ice thickness distributions. These control the sea-level response at later times of the climate scenarios, as Fig. 10 illustrates.

In addition to this intra-model variability, uncertainty in the sea-level projections arises from the temperature forcing. A comparison of the two sources of uncertainty for the years 2100 and 2500 of the ECP-8.5 scenario (Fig. 11) shows that they are of similar importance throughout the simulations. Via the procedure described in Sect. 3.3, we derive a combined uncertainty distribution for each scenario from which we can

TCD
6, 673–714, 2012

compute the likely (given by the 33rd and 66th percentiles) and very likely (given by the 5th and 95th percentiles) ranges of ice loss. Figure 12a shows the 972 projections of warming-induced ice loss from Antarctica. The uncertainty ranges are given separately for each scenario in Figs. 12b–e. While the rate of warming reaches its maximum within the 21st century (see Fig. 4), the dynamic response results only in a few centimeters sea-level rise until 2100. Warming-induced ice loss and the associated uncertainty thereafter increase with stronger climate forcing. The sea-level response is qualitatively similar for the scenarios ECP-4.5, 6.0 and 8.5. While the Antarctic mean temperature stabilizes after 2250 for each of these scenarios, the ice-sheet continues to lose mass thereafter, and increasingly so. By contrast, in the ECP-2.6 scenario, the ice-sheet tends towards a new stable state: After 2300, solid ice discharge decreases, following the decrease in temperature which sets in within the 21st century.

The delay in the ice response is not caused by the time-lag we have applied to the ocean warming. Figure 13 demonstrates that this time-lag in the forcing has little influence on the dynamic ice loss. Until 2100, the ice-loss curves for the simulations with and without time-lag in the ocean warming (in Fig. 13b shown exemplarily for one parameter combination picked from the model-spread) are almost identical. In 2500, the medians of the model spread differ by only 0.06 m, equivalent to approximately 3 % of the overall ice loss (see Fig. 13a).

The difference in ocean warming between the scenarios can lead to a qualitative change in the state of the Antarctic Ice Sheet: While the lateral boundaries remain at their initial position for the peak- and decline scenario ECP-2.6, both the grounding line as well as the calving fronts for major ice shelves retreat in the ECP-8.5 scenario. The high emission scenarios even lead to a disintegration of Ross Ice Shelf starting in the 23rd century, as shown exemplarily for one ensemble member in Fig. 14.

4.3 Ocean and surface warming including precipitation increase

The contribution of the Antarctic Ice Sheet to future sea-level rise highly depends on the changes in its surface mass balance.

TCD
6, 673–714, 2012

In a warming atmosphere we expect precipitation to increase as a consequence of the higher water vapor carrying capacity (Allen & Ingram, 2002; Uotila et al., 2007). In PISM-PIK, precipitation changes are computed according to the parameterization introduced by Huybrechts & Wolde (1999, Appendix C) based on the changes in temperature above the surface inversion layer. We neglect surface melting in our simulations since it is projected to remain comparably small even in strong climate change scenarios (Vizcaino et al., 2010; Huybrechts et al., 2011).

Under the ECP scenarios, precipitation generally increases, especially near the ice-sheet margins, where the surface air temperature, depending both on latitude and ice surface elevation, is highest. Averaged over the area of grounded ice in Antarctica, the increase in precipitation cumulates to 0.2 to 2.5 m sea-level equivalent in 2500 (see Fig. 15a). This is consistent with the results obtained from the CMIP3-AOGCMs via the scaling approach by Frieler et al. (2011). Figure 15b shows the cumulative precipitation changes modelled with PISM-PIK based on the parameterization by Huybrechts & Wolde (1999) in comparison to the cumulative precipitation changes computed using a method analogous to the one described for the surface temperature anomalies in Sect. 3.1.

Including the increase in precipitation projected for the ECP scenarios in our simulations generally leads to a change from sea-level rise to net sea-level drop (see Fig. 16a). As precipitation changes are directly linked to surface temperature changes, the same time-delay between forcing and the dynamic response of the ice-sheet applies, resulting in sea-level drop of only a few centimeters within the 21st century.

In the subsequent centuries, sea-level further drops, dependent on the magnitude in forcing: In 2500, the median of the uncertainty distributions derived as decribed in Sect. 3.3 ranges from −0.08 m for the ECP-2.6 to −0.56 m for the ECP-8.5 scenario (Figs. 16b–e).

From 2250 onwards, the effect of negative sea-level contribution caused by enhanced precipitation strongly decelerates. For a few of the ensemble members, it is even reversed, in case of the ECP-2.6 scenario leading to a sea-level change of essentially

TCD
6, 673–714, 2012

zero until 2500. Continuing these projections into the far future might lead to net sea-level rise despite the increase in precipitation. In general, the sea-level drop is significantly smaller than the sea-level equivalent of the cumulative precipitation (given in Fig. 15a), since part of the latter is compensated by a strong increase in dynamic ice loss (Fig. 17).

4.4 Role of ice-sheet history

In the projections above, we have observed that solid ice loss generally differs very little within the 21st century both across the model-spread and across the different scenarios (see Figs. 9, 12 and 17). We have shown that the delay in the ice response does not result from the time-lag in the applied ocean-warming (see Fig. 13). Initializing from the equilibrium state and applying the forcing only after 200 years of run-time does not yield a difference in the results, suggesting that this is not due to a numerical initialization issue, but that there is a physical cause for the time-delay between forcing and ice response. A possible reason could be that ice-dynamical changes rather follow the aggregated climate forcing than being an immediate response to warming or precipitation increase.

PISM-PIK is able to reproduce the magnitude of currently observed rates and acceleration of solid ice loss. However, we find the corresponding values only in later years of the simulations. Figure 18a shows the acceleration of ice loss under the ECP scenarios. For comparison, we give the observational value of $9\,\mathrm{Gt\,yr^{-2}}$ found by Rignot et al. (2011) for the period 1992–2009. The simulations first coincide with this value in the time-period between 2068 and 2085 under the strongest scenarios ECP-8.5. We first find the associated solid ice discharge in the year 2011 of the highest emission scenario (see Fig. 18b).

The geometries of the Antarctic ice-sheet associated with these years hardly differ from the initial state of the simulation. Figure 19 shows that the ice thickness anomalies for the years 2011 and 2077 of the ECP-8.5 scenario to the equilibrium state are only of the order of a few meters. The positions of the grounding line and ice fronts appear

TCD
6, 673–714, 2012

to be stable within this timeframe albeit we have shown it to be very sensitive to enhanced basal melting in later years of the simulation (Fig. 14). In conclusion, we find no quantitative criterion for a clear distinction between the equilibrium state and a state of the ice-sheet preceding strong dynamical changes.

However, the indistinguishable states from the years 2000 and 2077 give rise to significantly different solid ice discharge: While dynamic ice loss caused by warming and precipitation increase amounts to at most 0.07 m within the 21st century, it reaches approximately 0.24 m within the century succeeding 2077, a year picked from the time-period for which the modelled acceleration first matches the observed value (see Fig. 18c).

We conclude that the history of the ice-sheet plays a crucial role with regards to its future contribution to sea-level rise, inducing an additional uncertainty in sea-level projections next to ones introduced by the model parameters and the temperature evolution for a given emission scenario.

5 Conclusions

In this paper, we have studied the response of the Antarctic Ice Sheet to warming and precipitation increase under the Extended Concentration Pathways with the Potsdam Parallel Ice Sheet Model PISM-PIK, with special focus on the uncertainty induced by the climate projections as well as ice-physics parameters.

PISM-PIK has a continuous representation of the dynamics in sheet, shelves and the transition zone and includes the processes which are most relevant for investigating solid ice discharge from Antarctica. One improvement in comparison to some other ice-sheet models which have been used in previous studies of future sea-level rise from Antarctica is the incorporation of ice-shelf dynamics. Grounding line migration is strongly affected by changes in ice-shelf buttressing (in PISM-PIK governed by the calving law introduced in Levermann et al. (2011)) as well as sub-shelf melting. Modelling sub-shelf melt rates was incorporated by use of the ocean-box model by Olbers & Hellmer (2010) which enables the model to reproduce observed basal melt rates of major Antarctic ice shelves as well as to project melt rates for future scenarios.

TCD
6, 673–714, 2012

The future solid ice discharge from Antarctica has been investigated in three types of experiments, consecutively adding the effects of surface warming, ocean warming and enhanced precipitation. For the ECP-8.5 scenario, corresponding to a warming of about 11 °C, the maximum dynamic ice loss from Antarctica is 0.58 m in the case of surface warming only. Enhanced sub-shelf melting causes additional ice loss, leading to a maximum sea-level rise of 1.03 m until 2500. In the high emission scenarios, the rise in sub-shelf melting also causes a significant change in the position of the grounding-line and calving fronts and eventually leads to the disintegration of Ross Ice Shelf. Increased precipitation dominates the mass balance, and leads to a change from net sea-level rise to sea-level drop. However, this goes along with an increase in solid ice loss, which counteracts the ice gain through precipitation. This results in a deceleration of sea-level drop within the 23rd century in the simulations with full climate forcing. The implications for long-term projections need to be further investigated, especially the question whether an increase in precipitation necessarily leads to an increase in ice volume.

Our results show that it is essential to include the different sources of uncertainty in future sea-level projections. These comprise the climate uncertainty as well as the intra-model uncertainty which we have shown to be of similar importance in our simulations.

Furthermore, we find that the history of the ice-sheet plays an important role with respect to its future contribution to sea-level rise. This is apparent from the fact that very similar states of the Antarctic Ice Sheet can give rise to significantly different changes in dynamic ice loss, leading to sea-level rise of 0.24 m in contrast to 0.07 m in the subsequent century. This crucial role of the initial state needs to be kept in mind in the context of sea-level projections.

In all experiments, we observe a time-delay between climate forcing and ice-sheet response, such that the sea-level signal within the 21st century is small, even for the strongest warming scenarios. This could be due to the rather coarse resolution in PISM-PIK with which many structures in the ice cannot be resolved, including narrow

TCD
6, 673–714, 2012

ice streams which might contribute significantly to the overall ice discharge. In PISM-PIK, basal friction is computed using a simple parameterization which only depends on the topography and ice thickness. We expect a significant improvement of the results by including a thermodynamic model to better represent basal sliding which is crucial for the ice flux across the grounding line. It should be noted that strong acceleration of the ice discharge, as observed in satellite data (Rignot et al., 2011), can be found in our simulations. It occurs as a trend under strong warming scenarios, but also as variability after the 21st century. This shows that the model is in principle capable of such fast dynamics. Simulations presented here do not allow to decide whether the observed signal was caused by variability in the ice-ocean system or by a persistent warming trend.

Acknowledgements. This study was funded by the German Federal Ministry of Education and Research (BMBF) and by SURVIVE (grant 11_II_093_Global_A_SIDS and LDCs). We thank Matthias Mengel for interesting discussions on the paper. RW acknowledges support by the IMPRS-ESM.

References

Albrecht, T., Martin, M., Haseloff, M., Winkelmann, R., and Levermann, A.: Parameterization for subgrid-scale motion of ice-shelf calving fronts, The Cryosphere, 5, 35–44, doi:10.5194/tc-5-35-2011, 2011. 675

Allen, M.R., and Ingram, W.J.: Constraints on future changes in climate and the hydrologic cycle, Nature, 419, 224–232, 2002. 685

Applegate, P. J., Kirchner, N., Stone, E. J., Keller, K., and Greve, R.: Preliminary assessment of model parametric uncertainty in projections of Greenland Ice Sheet behavior, The Cryosphere Discuss., 5, 3175–3205, doi:10.5194/tcd-5-3175-2011, 2011. 675

Bindschadler, R. et al.: SeaRISE, Sensitivities of Earth's Ice Sheets to their Environments, http://websrv.cs.umt.edu/isis/index.php/SeaRISE_Assessment, in preparation, 2012. 677

Frieler, K., Meinshausen, M., Mengel, M., Braun, N., and Hare, W.: A scaling approach to probabilistic assessment of regional climate change, J. Climate, doi:10.1175/JCLI-D-11-00199.1, accepted, 2011. 678, 679, 685

TCD
6, 673–714, 2012

Giorgi, F.: A simple equation for regional climate change and associated uncertainty, J. Climate, 21, 1589–1604, 2008. 678
Grosfeld, K., Schroeder, M., Fahrbach, E., Gerdes, R., and Mackensen, A.: How iceberg calving and grounding change the circulation and hydrography in the Filchner Ice Shelf-Ocean System, J. Geophys. Res., 106, 9039–9055, 2001. 680
Hellmer, H. H., Jacobs, S. S., and Jenkins, A.: Oceanic erosion of a floating Antarctic glacier in the Amundsen Sea, in: Ocean, ice and atmosphere: interactions at Antarctic Continental margin, vol 75 of Antarctic research series, edited by: Jacobs, S. S., Weiss, R., American Geophysical Union, Washington, DC, 83–100, 1998. 680
Huybrechts, P. and Wolde, J. De.: The Dynamic Response of the Greenland and Antarctic Ice Sheets to Multiple-Century Climatic warming, J. Climate, 12, 2169–2188, 1999. 685, 710
Huybrechts, P., Grerory, J., Janssens, I., and Wild, M.: Modelling Antarctic and Greenland volume changes during the 20th and 21st centuries forced by GCM time slice integrations, Global Planet. Change, 42, 83–105, 2004. 675
Huybrechts, P., Goelzer, H., Janssens, I., Driesschaert, E., Fichefet, T., Goosse, H., and Loutre, M.-F., Response of the Greenland and Antarctic Ice Sheets to Multi-Millennial Greenhouse Warming in the Earth System Model of Intermediate Complexity LOVECLIM, Surv. Geophys., 32, 397–416, 2011. 675, 685
Jacobs, S. S. and Giulivi, C. F.: Interannual ocean and sea ice variability in the Ross Sea, in: Ocean, ice and atmosphere: Interactions at Antarctic Continental margin, vol 75 of Antarctic research series, edited by: Jacobs, S. S., Weiss, R., American Geo- physical Union, Washington, DC, 1998. 680
Le Brocq, A. M., Payne, A. J., and Vieli, A.: An improved Antarctic dataset for high resolution numerical ice sheet models (ALBMAP v1), Earth System Science Data, 2, 247–260, 2010. 677
Levermann, A., Albrecht, T., Winkelmann, R., Martin, M. A., Haseloff, M., and Joughin, I.: Kinematic first-order calving law implies potential for abrupt ice-shelf retreat, The Cryosphere Discuss., 5, 2699–2722, doi:10.5194/tcd-5-2699-2011, 2011. 675, 687
Ma, Y., Gagliardini, O., Ritz, C., Gillet-Chaulet, F., Durand, G., and Montagnat, M.: Enhancement Factors for Grounded Ice and Ice-Shelves inferred from an anisotropic ice flow model, J. Glaciol., 56, 805–812, 2010. 677
Martin, M. A., Winkelmann, R., Haseloff, M., Albrecht, T., Bueler, E., Khroulev, C., and Levermann, A.: The Potsdam Parallel Ice Sheet Model (PISM-PIK) Part 2: Dynamic equilibrium

TCD
6, 673–714, 2012

simulation of the Antarctic ice sheet, The Cryosphere, 5, 727–740, doi:10.5194/tc-5-727-2011, 2011. 675, 677, 679

Martin, M. A., Winkelmann, R., Ligtenberg, S. R. M., van den Broeke, R. M., and Levermann, A.: Parameter sensitivity of dynamic ice loss in Antarctica: SeaRise experiments with the Parallel Ice Sheet Model, PISM, in preparation, 2012. 675, 677

Meehl, G. A., Covey, C., Delworth, T., Latif, M., McAvaney, B., Mitchell, J. F. B., Stouffer, R. J., and Taylor, K. E.: THE WCRP CMIP3 Multimodel Dataset: A New Era in Climate Change Research, B. Am. Meteorol. Soc., 88, 1383, 2007. 679

Meehl, G. A., Stocker, T. F., Collins, W. D., Friedlingstein, P., Gaye, A. T., Gregory, J. M., Kitoh, A., Knutti, R., Murphy, J. M., Noda, A., Raper, S. C. B., Watterson, I. G., Weaver, A. J., and Zhao, Z.-C.: Climate Change 2007: The Physical Science Basis, Contribution of Working Group I to the Fourth Assessment Report of the Intergovernmental Panel on Climate Change, chap. Global Climate Projections, edited by: Solomon, S., Qin, D., Manning, M., Chen, Z., Marquis, M., Averyt, K. B., Tignor, M. and Miller, H. L., Cambridge University Press, Cambridge, United Kingdom and New York, USA, 2007. 674

Meinshausen, M., Meinshausen, N., Hare, W., Raper, S. C. B., Frieler, K., Knutti, R., Frame, D. J., and Allen, M, R.: Greenhouse-gas emission targets for limiting global warming to 2 ˚C , Nature, 458, 1158–1162, 2009. 678

Meinshausen, M., Raper, S. C. B., and Wigley, T. M. L.: Emulating coupled atmosphere-ocean and carbon cycle models with a simpler model, MAGICC6 Part 1: Model description and calibration, Atmos. Chem. Phys., 11, 1417–1456, doi:10.5194/acp-11-1417-2011, 2011a. 678

Meinshausen, M., Smith, S., Calvin, K., Daniel, J., Kainuma, M., Lamarque, J.-F., Matsumoto, K., Montzka, S., Raper, S., Riahi, K., Thomson, A., Velders, G., and van Vuuren, D. P.: The RCP greenhouse gas concentrations and their extensions from 1765 to 2300, Climatic Change, 109, 213–241, doi:10.1007/s10584-011-0156-z, 2011b. 675, 678

Nicholls, K. W., Padman, L., Schroeder, M., Woodgate, R. A., Jenkins, A., and Osterhus, S.: Water mass modication over the continental shelf north of Ronne ice shelf, Antarctica, J. Geophys. Res., 108, 3260, 2003. 680

Olbers, D. and Hellmer, H.: A box model of circulation and melting in ice shelf caverns, Ocean Dynam., 60, 141–153, 2010. 675, 680, 687, 695, 696, 701

Payne, A. J., Holland, P. R., Shepherd, A. P., Rutt, I. C., Jenkins, A., and Joughin, I.: Numerical modeling of ocean-ice interactions under Pine Island Bay's ice shelf, J. Geophys. Res., 112,

14 pp. , 2007. 679
PISM-authors: PISM, a Parallel Ice Sheet Model: User's manual, http://www.pism-docs.org/wiki/lib/exe/fetch.php?media=manual.pdf, 2012. 677
Rignot, E. and Jacobs, S. S.: Rapid Bottom Melting Widespread near Antarctic Ice Sheet Grounding Lines, Science, 296, doi:10.1126/science.1070942, 2002. 679
Rignot, E., Velicogna, I., van den Broeke, M. R., Monaghan, A., and Lenaerts, J.: Acceleration of the contribution of the Greenland and Antarctic ice sheets to sea level rise, GRL, 38, 5503, 2011. 674, 686, 689, 713, 714
Schewe, J., Levermann, A., and Meinshausen, M.: Climate change under a scenario near 1.5°C of global warming: monsoon intensification, ocean warming and steric sea level rise, Earth System Dynamics, 2, 25–35, 2011. 678
SeaRISE: Sea-level Response to Ice Sheet Evolution (SeaRISE), 2011. 677
Uotila, P., Lynch, A. H., Cassano, J. J., and Cullather, R. I.: Changes in Antarctic net precipitation in the 21st century based on Intergovernmental Panel on Climate Change (IPCC) model scenarios, J. Geophys. Res., 112, 10107, 2007. 674, 685
van Vuuren, D., Edmonds, J., Kainuma, M., Riahi, K., Thomson, A., Hibbard, K., Hurtt, G., Kram, T., Krey, V., Lamarque, J.-F., Masui, T., Meinshausen, M., Nakicenovic, N., Smith, S., and Rose, S.: The representative concentration pathways: an overview, Climatic Change, 109, 5–31, doi:10.1007/s10584-011-0148-z, 2011. 678
Vizcaino, M., Mikolajewicz, U., Gröger, M., Maier-Reimer, E., Schurgers, G., and Winguth, A. M. E.: Long-term ice sheetclimate interactions under anthropogenic greenhouse forcing simulated with a complex Earth System Model, Clim. Dynam., 31, 665–690, 2008. 675
Vizcaino, M., Mikolajewicz, U., Jungclaus, J., and Schurgers, G.: Climate modification by future ice sheet changes and consequences for ice sheet mass balance, Clim. Dynam., 34, 301–324, 2010. 675, 685
Winkelmann, R., Martin, M. A., Haseloff, M., Albrecht, T., Bueler, E., Khroulev, C., and Levermann, A.: The Potsdam Parallel Ice Sheet Model (PISM-PIK) Part 1: Model description, The Cryosphere, 5, 715–726, doi:10.5194/tc-5-715-2011, 2011. 675, 676
Wong, A. P. S., Bindoff, N. L., and Forbes, A.: Ocean-ice shelf inter-action and possible bottom water formation in Prydz Bay, Antarctica, in: Ocean, ice and atmosphere: interactions at Antarctic Continental Margin, vol 75 of Antarctic Research Series, edited by: Jacobs, S. S., Weiss, R., American Geophysical Union, Washington, DC, 173–187, 1998. 680

TCD
6, 673–714, 2012

Table 1. Table of parameter variations for the enhancement factors E_{SIA} and E_{SSA} and the porewater fraction F_p. From all possible combinations we exclude those for which the geometry of the Antarctic Ice Sheet in an equilibrium simulation with present-day boundary conditions deviates strongly from current observations.

Parameter	Variation
E_{SIA}	4.5, 5.0, 5.5
E_{SSA}	0.3, 0.4, 0.5, 0.6, 0.7, 0.8, 0.9
F_p	89 % , 90 % , 91 % , 92 % , 93 % , 94 % , 95 % , 96 % , 97 % , 98 % , 99 %

TCD
6, 673–714, 2012

Table 2. Scaling coefficients for the ocean temperature anomalies. For each CMIP3-AOGCM we selected the time-lag providing the highest correlation. (The respective correlation coefficients are given in column r^2.) For each region, we then chose the model with the highest scaling coefficient between the ocean temperature and the global mean temperature, given in column $\overline{\Delta T_o}/\overline{\Delta T_g}$.

Region	AOGCM	$\overline{\Delta T_o}/\overline{\Delta T_g}$	Time-lag [yrs]	r^2
Amery	Canadian Centre for Climate Modelling and Analysis Coupled General Circulation Model, version 3.1	0.77	60	0.97
Filchner-Ronne	Model for Interdisciplinary Research on Climate, high-resolution version, version 3.2	0.38	20	0.94
Pine Island Glacier	Goddard Institute for Space Studies Model E-H	0.77	85	0.89
Ross	Canadian Centre for Climate Modelling and Analysis Coupled General Circulation Model, version 3.1	0.55	65	0.93

TCD
6, 673–714, 2012

Table 3. Table of initial temperatures and salinities used for the computation of basal melt rates based on the ocean box model by Olbers & Hellmer (2010). B_0 denotes the ocean box at the cavern entrance.

Ice shelf	Initial temperature in B_0 [°C]	Initial salinity in B_0 [psu]
Amery (AIS)	−1.83	34.55
Filchner-Ronne (FRIS)	−1.84	34.74
Pine Island Glacier (PIG)	+0.84	34.67
Ross (RIS)	−1.85	34.83

TCD
6, 673–714, 2012

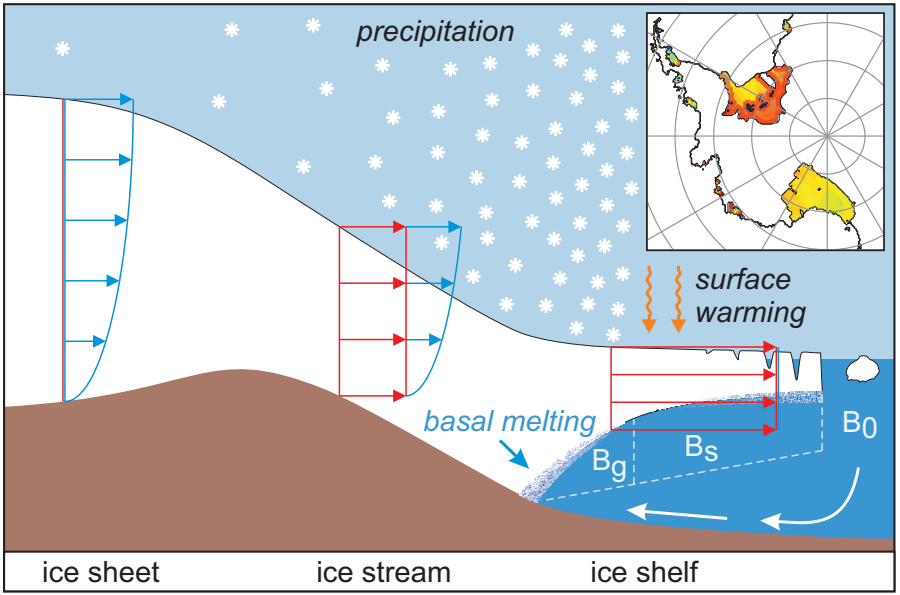

Fig. 1: Conceptual figure illustrating the climate forcing acting on ice sheet and shelves and the velocity patterns associated with the different flow regimes (vertical SIA-velocity profile in blue and depth-independent SSA-velocity in red). Basal melting and refreezing are modeled using the equilibrium solutions of the ocean box model by Olbers & Hellmer (2010). To this end, each sub-shelf cavern is divided into ocean box B_g which is close to the grounding line and covers about one third of the ice shelf base, and ocean box B_s which comprises the rest of the shelf base and borders the reservoir box B_0. The resulting melt patterns for the shelves of the West Antarctic Ice Sheet as modeled with PISM-PIK are displayed in the inlay. Generally, melt rates are higher towards the grounding line, refreezing only occurs near shelf fronts. The highest basal melt rates are found for the shelf attached to Pine Island Glacier.

TCD
6, 673–714, 2012

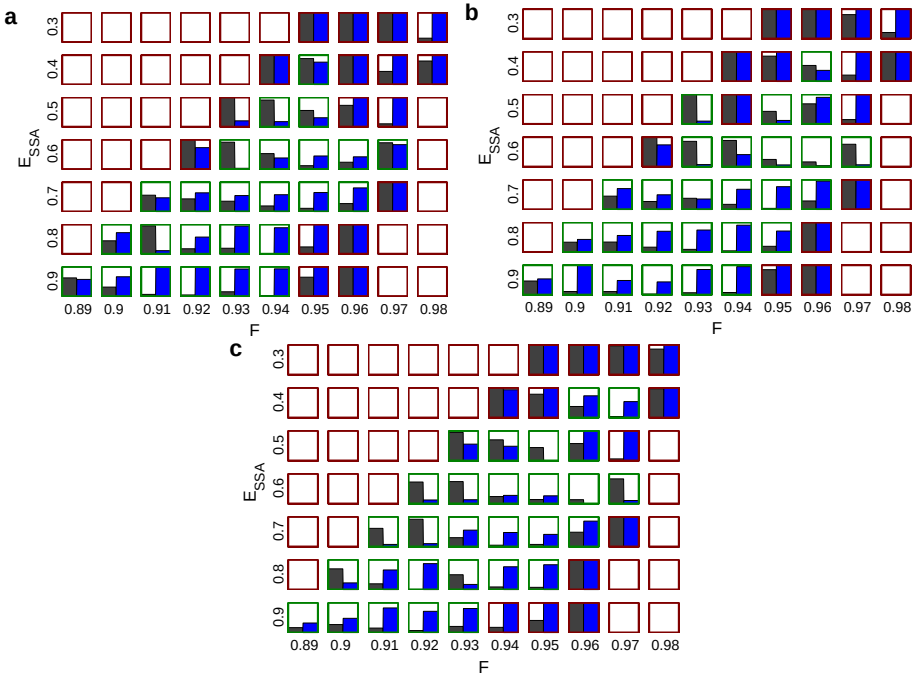

Fig. 2: Parameter combinations of the perturbed-physics ensemble for $E_{\mathrm{SIA}} = 4.5$ (Panel a), $E_{\mathrm{SIA}} = 5.0$ (Panel b) and $E_{\mathrm{SIA}} = 5.5$ (Panel c). For each parameter combination, the deviation in ice volume above floatation and ice-shelf area up to 10 % of the observations are given in gray and blue, respectively. If one of these thresholds is exceeded, the combination is excluded from the ensemble. The remaining 81 parameter combinations are indicated by green borders.

TCD
6, 673–714, 2012

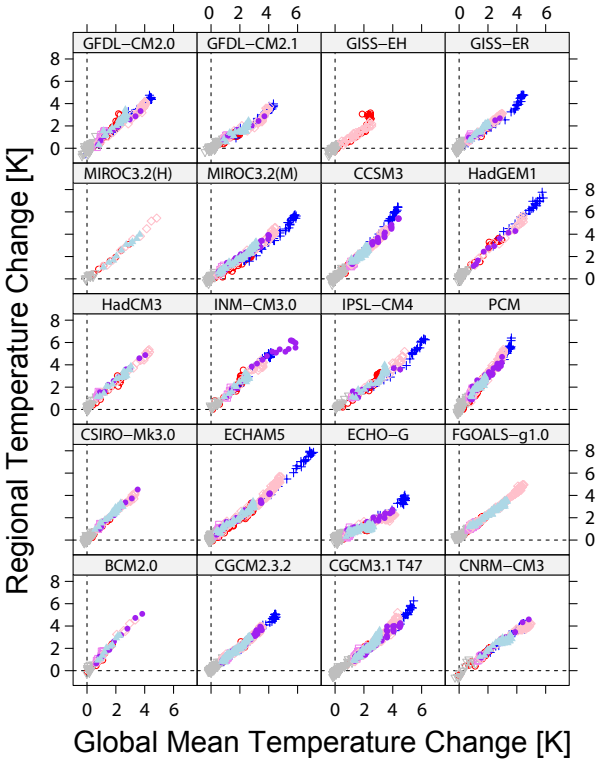

Fig. 3: Ten-year averages of annual temperature changes over the Antarctic Ice Sheet, plotted against global-mean temperature change for 20 CMIP3-AOGCMs. Changes refer to pre-industrial forcing conditions. Different colors indicate different scenarios: Red represents an idealized scenario assuming increasing CO2 concentrations of 1 % per year up to doubled levels, blue an idealized scenario assuming increasing CO2 concentrations of 1 % per year up to quadrupled levels, gray a twentieth-century run, violet a commitment simulation where concentrations are kept constant at the year 2000 levels, pink represents the SRES-A1B scenario, purple the SRES-A2 scenario, and light blue the SRES-B1 scenario.

TCD
6, 673–714, 2012

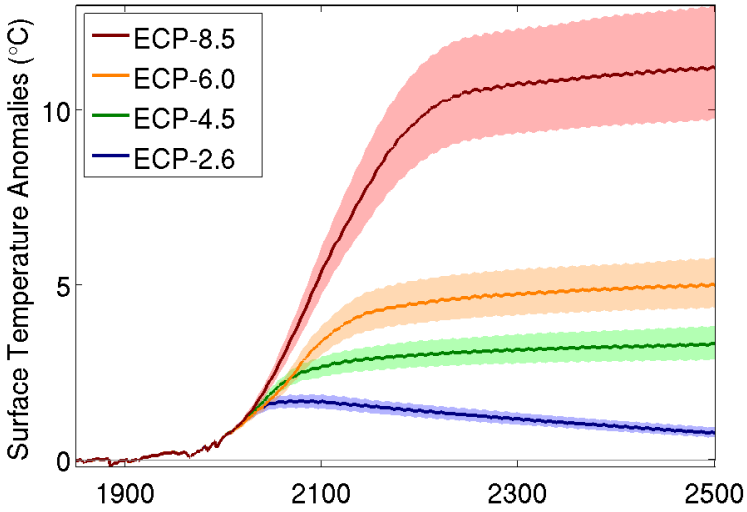

Fig. 4: Antarctic surface temperature anomalies for the ECP scenarios, generated as described in Sect. 3.1. Given are the median (solid lines) compared to the likely range (shading, defined by the 33rd and 66th percentiles of the uncertainty distribution). The small temporal variations are caused by the 11-year solar cycle.

TCD
6, 673–714, 2012

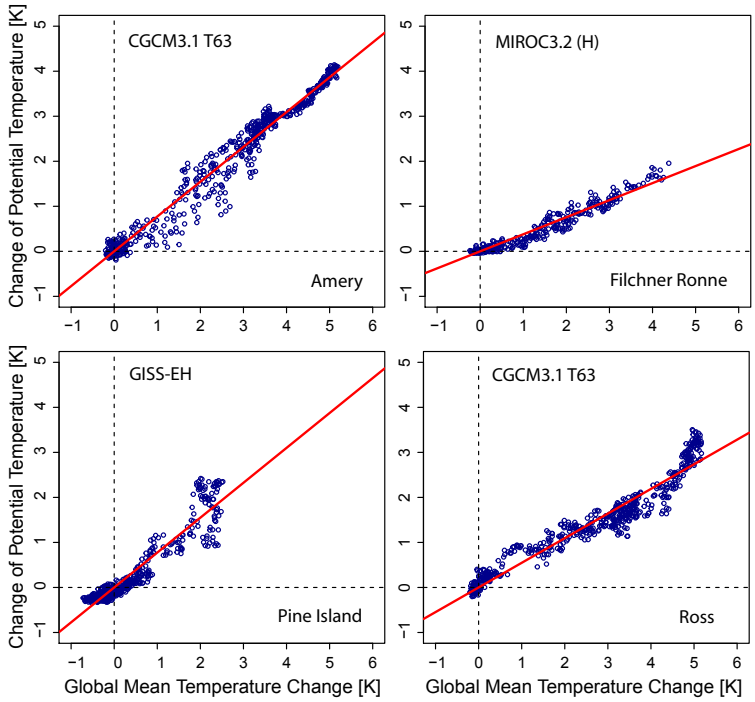

Fig. 5: Annual mean ocean temperature changes for the Amery, Filchner-Ronne, Pine-Island and Ross regions, plotted against global-mean temperature change for the selected CMIP3-AOGCMs. Temperatures are averaged at a depth of 450 to 550 m for the Amery region, 200 to 350 m for the Filchner-Ronne region, 400 to 600 m for the Pine-Island region and 450 to 550 m for the Ross region along the coastal segments of the respective ice shelves.

TCD
6, 673–714, 2012

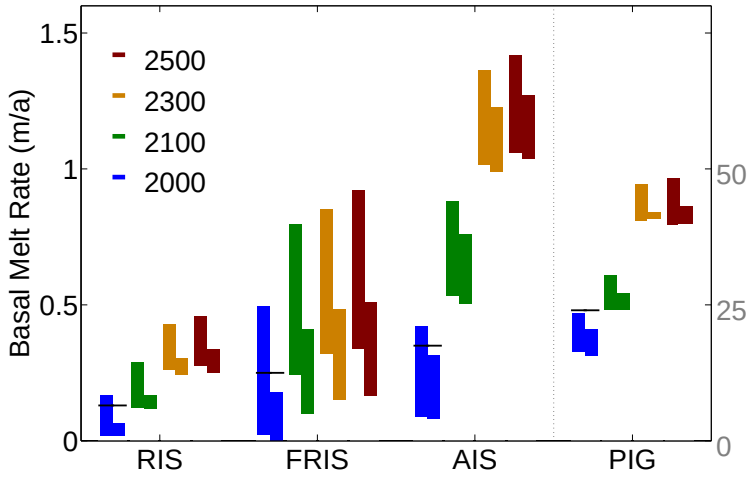

Fig. 6: Basal melt rates in 2000, 2100, 2300 and 2500 of the ECP-4.5 scenario. In each column, the left bar shows the melt rates for ice in contact with B_g, the right bar for ice in contact with B_s. Melt rates near the grounding line are generally higher than at the rest of the ice-shelf base. Observed melt rates (black lines, see Olbers & Hellmer (2010)) are within the modelled ranges for the year 2000. Note that all values for PIG are scaled in this plot by a factor of 0.02 – the respective scale is given on the right.

TCD
6, 673–714, 2012

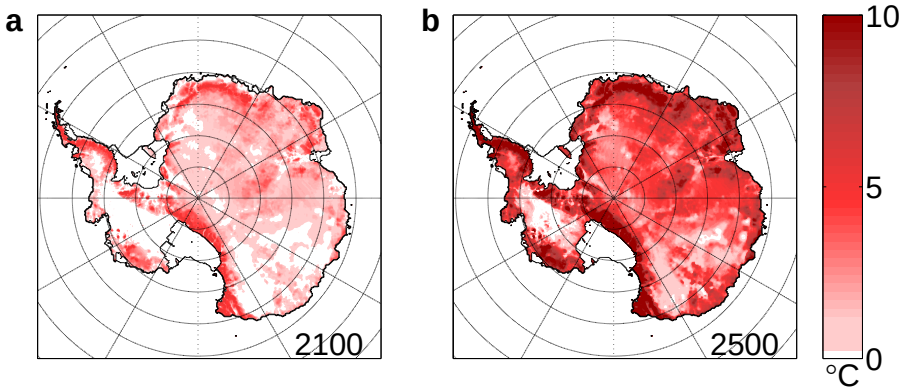

Fig. 7: Vertically-averaged ice temperature anomalies for the years 2100 (Panel a) and 2500 (Panel b) of the ECP-8.5 scenario. While the surface temperature anomaly is applied uniformly, the vertically-averaged temperature anomaly is altered by the heat transport processes within the ice.

TCD
6, 673–714, 2012

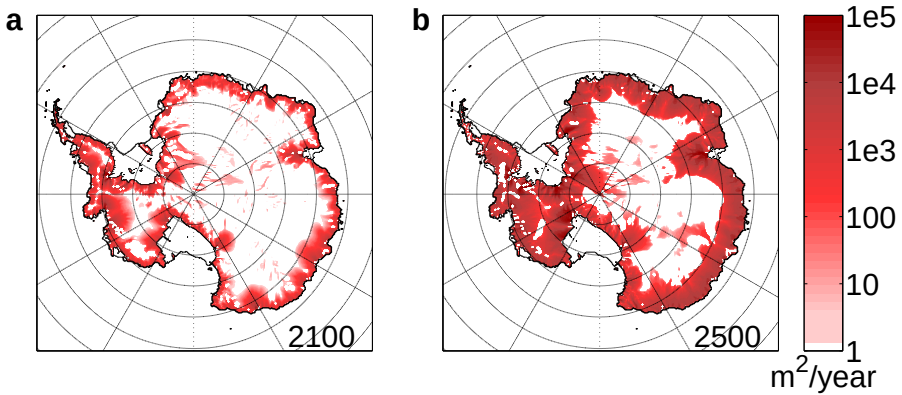

Fig. 8: Vertically-averaged increase in ice-flux for the years 2100 (Panel a) and 2500 (Panel b) of the ECP-8.5 scenario.

TCD
6, 673–714, 2012

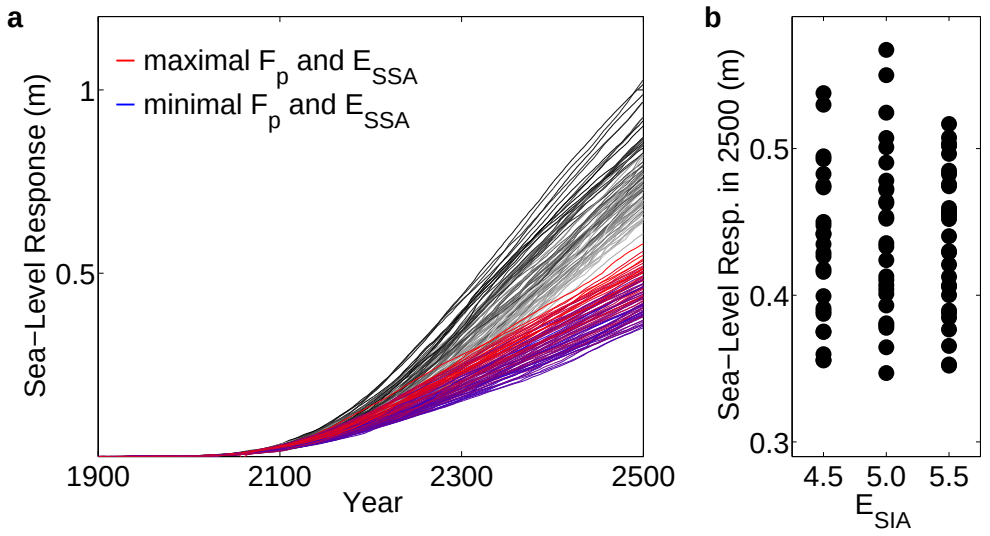

Fig. 9: Panel **a** Dynamic ice loss of Antarctica under the ECP-8.5 scenario for surface warming only, given in meters sea-level equivalent. For higher F_p and E_{SSA}, the color changes from blue to red. For comparison, the sea-level response to surface plus ocean warming is given in shades of gray (darker gray corresponding to higher F_p and E_{SSA}). Panel **b** Sea-level response in year 2500 of the ECP-8.5 scenario, plotted against parameter E_{SIA}. Within the time-scale of the scenarios, we observe no clear dependence on this parameter.

TCD
6, 673–714, 2012

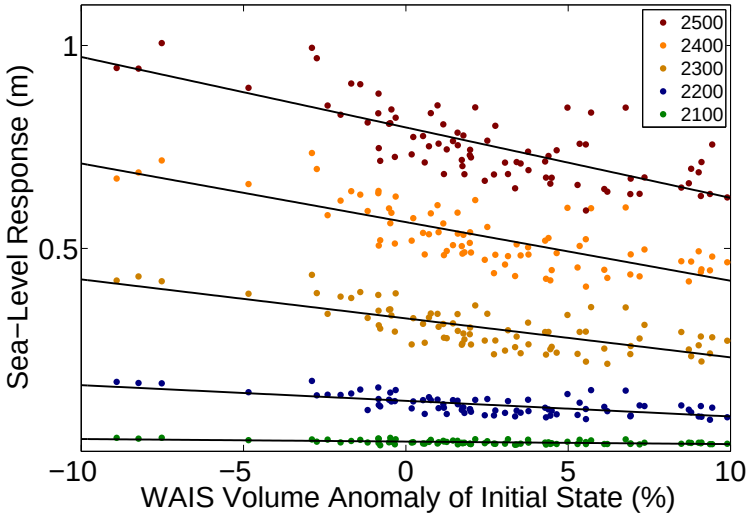

Fig. 10: Warming-induced ice loss for the ECP-8.5 scenario in meters sea-level equivalent. Each dot represents one of the 81 parameter combinations. Dynamic ice loss is almost independent of the initial sea-level relevant volume of the West Antarctic Ice Sheet up until year 2100 (green). For later years (2200 in blue, 2300 in yellow, 2400 in orange, 2500 in red), the parameter dependence manifests in an anti-correlation between ice loss and initial volume. For the weaker climate scenarios, the relation is qualitatively similar.

TCD
6, 673–714, 2012

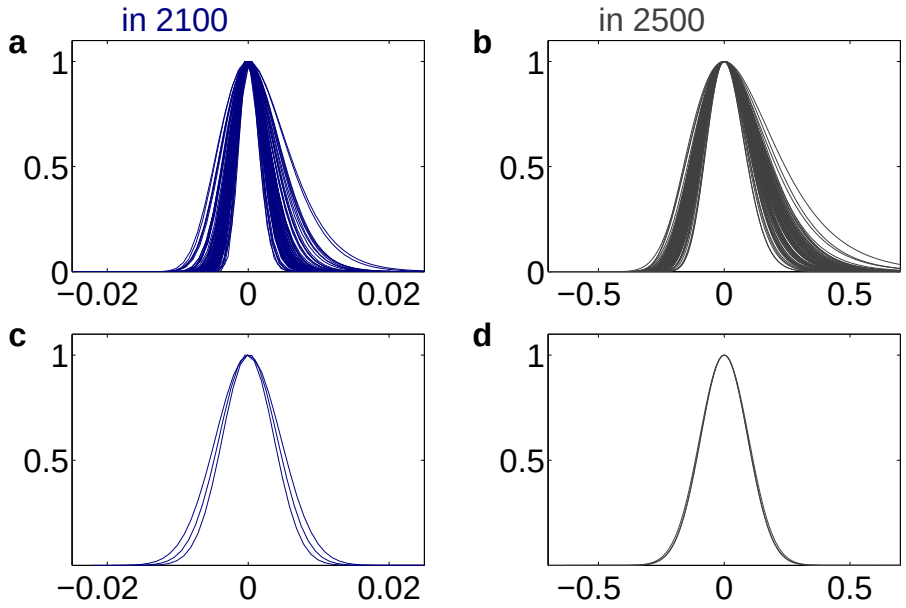

Fig. 11: Comparison of uncertainties. Panels **a–b** Climate uncertainty for the years 2100 and 2500. Provided are the probability distributions of ice loss through warming in the ECP-8.5 scenario for each ice parameter combination. Panels **c–d** Ice-parametric uncertainty for the years 2100 and 2500. Given are the probability distributions of ice loss through warming for the 33rd, 50th and 66th percentiles of the ECP-8.5 scenario. For better visualization, each uncertainty distribution is normalized to one in the vertical and shifted along the x-axis such that the mode coincides with zero.

TCD
6, 673–714, 2012

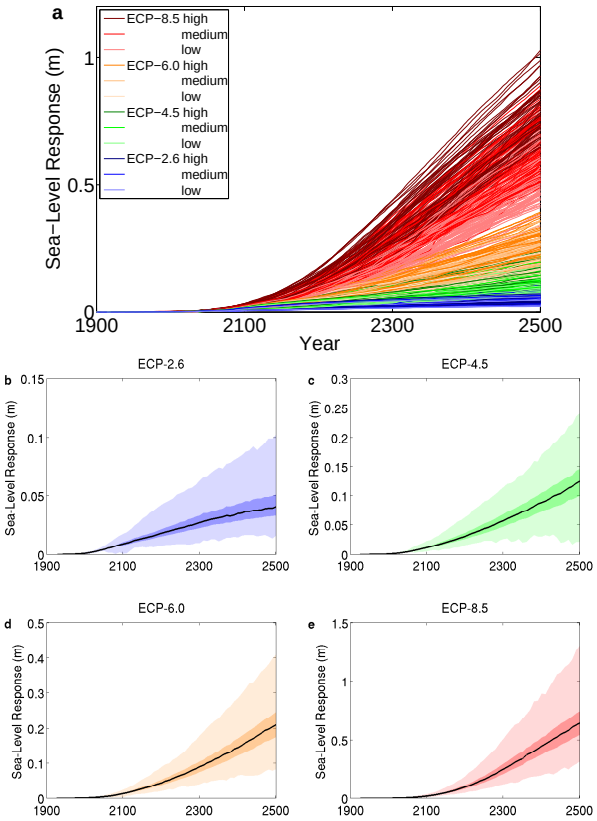

Fig. 12: Sea-level response of Antarctica to surface and ocean warming, given in meters sea-level equivalent. Panel **a** Sea-level projections from PISM-PIK for the temperature pathways corresponding to the 33rd (= low), 50th (= medium) and 66th (= high) percentiles of the temperature range projected for the ECPs. Each line correponds to one of the 81 realizations of the Antarctic Ice Sheet. Panels **b–e** Uncertainty ranges for each ECP scenario, comprising both the intra-model uncertainty and the uncertainty in the temperature projections. Given are the median (dark lines) and the likely (dark shading, defined by the 33rd and 66th percentiles) and very likely (light shading, defined by the 5th and 95th percentiles) ranges for the sea-level response. The computation of these ranges is detailed in Sect. 3.3.

TCD
6, 673–714, 2012

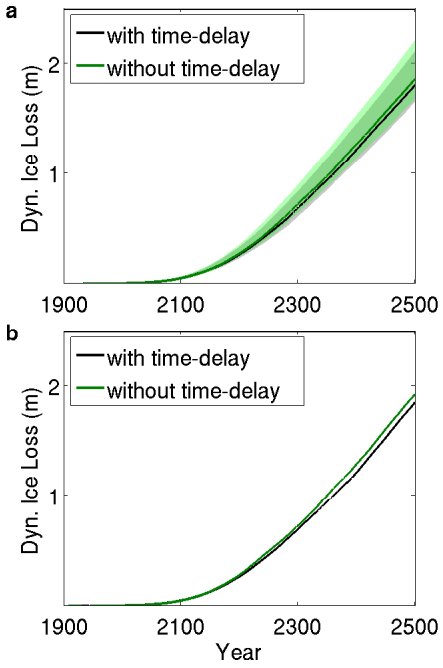

Fig. 13: Comparison of dynamic ice loss from Antarctica in simulations with (black) and without (green) time-lag in the ocean forcing. Panel **a** Dynamic ice loss for the upper emission scenario ECP-8.5, caused by surface warming, precipitation and ocean warming applied with (black) and without (green) time-lag. Solid lines show the median of the full parameter spread, given as shading. Panel **b** Dynamic ice loss as in Panel a, but for one parameter combination picked from the model spread, in order to show that the similarity of the simulations does not arise from a statistical effect, but is physically caused.

TCD
6, 673–714, 2012

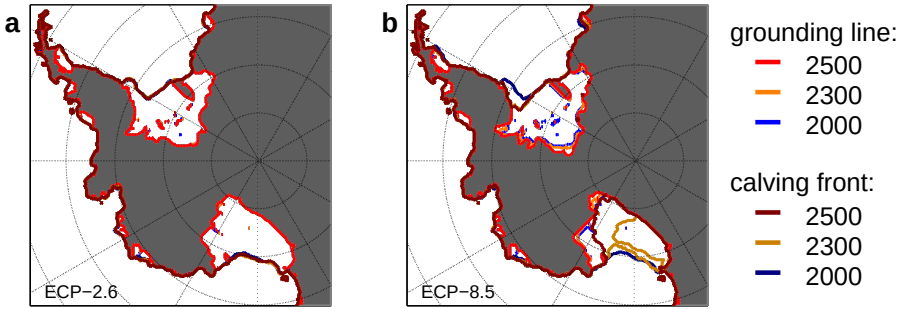

Fig. 14: Lateral boundaries for the years 2000, 2300 and 2500 of the scenarios ECP-2.6 (Panel a) and ECP-8.5 (Panel b). For the latter, Ross Ice Shelf disintegrates within in the 23rd century.

TCD
6, 673–714, 2012

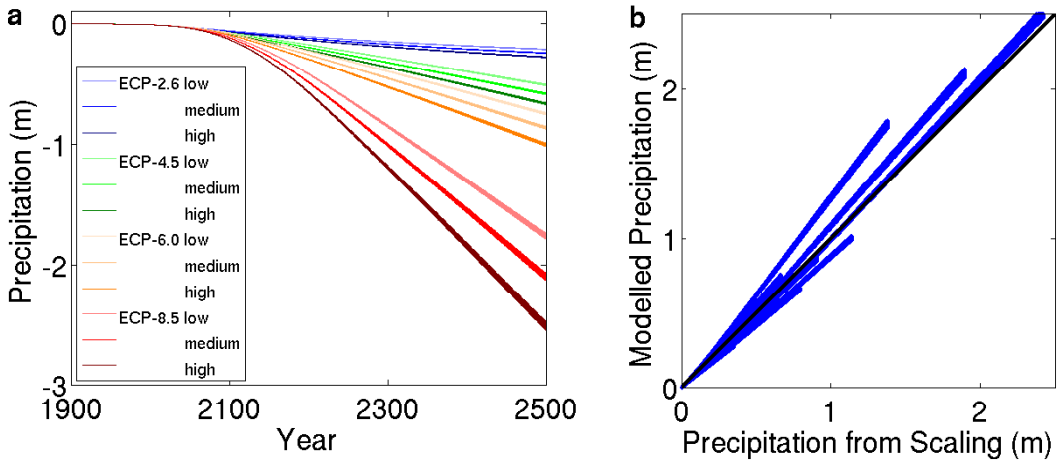

Fig. 15: Panel **a** Cumulative precipitation increase for the ECP scenarios, given in meters sea-level equivalent. Panel **b** Precipitation as modelled within PISM-PIK, based on the parameterization by Huybrechts & Wolde (1999), agrees well with the precipitation computed via the scaling approach from the results of 20 CMIP3-AOGCMs. Shown is the cumulative precipitation in meters sea-level equivalent, averaged over Antarctica, for each scenario and each member of the perturbed-physics ensemble. Black line indicates the identity.

TCD
6, 673–714, 2012

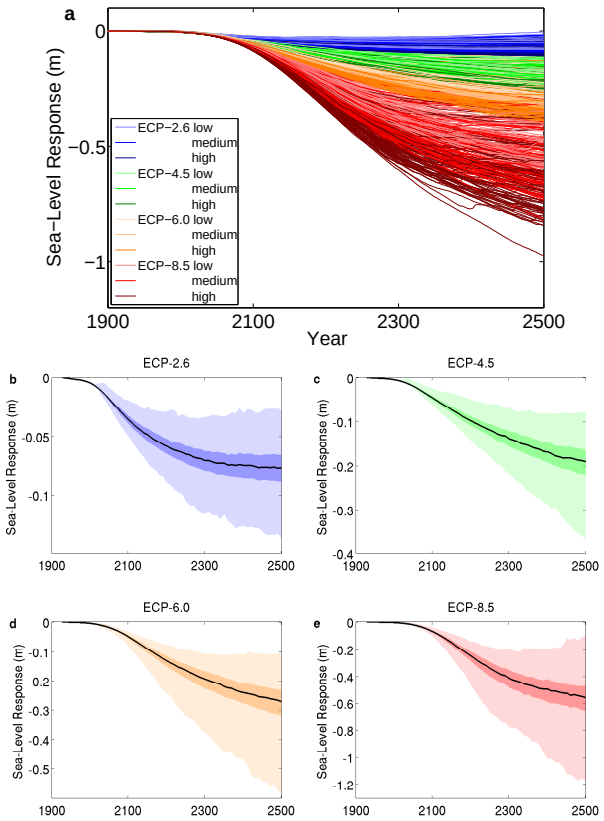

Fig. 16: Sea-level response of Antarctica to warming and precipitation increase, given in meters sea-level equivalent. Panel **a** Sea-level projections from PISM-PIK for the temperature pathways corresponding to the 33rd (= low), 50th (= medium) and 66th (= high) percentiles of the temperature range projected for the ECPs. Each line correponds to one of the 81 realizations of the Antarctic Ice Sheet. Panels **b–e** Uncertainty ranges for each ECP scenario, comprising both the intra-model uncertainty and the uncertainty in the temperature projections. Given are the median (dark lines) and the likely (dark shading, defined by the 33rd and 66th percentiles) and very likely (light shading, defined by the 5th and 95th percentiles) ranges for the sea-level response. The computation of these ranges is detailed in Sect. 3.3.

TCD
6, 673–714, 2012

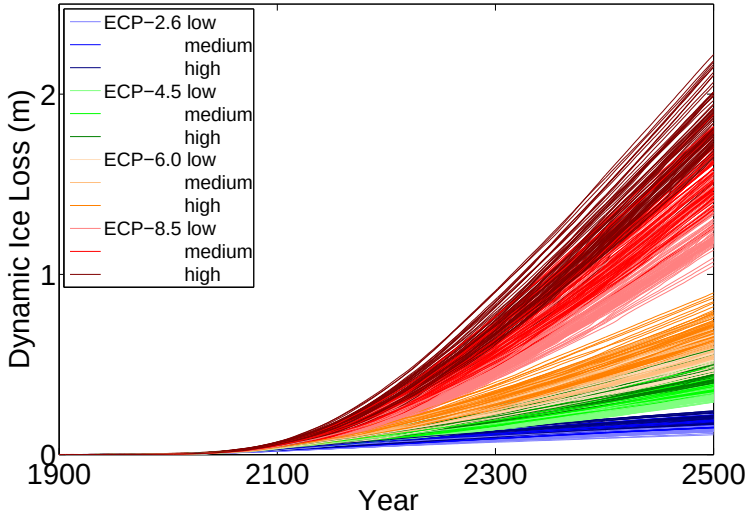

Fig. 17: Dynamic ice loss (in meters sea-level equivalent) of Antarctica caused by warming and precipitation increase for the temperature pathways corresponding to the 33rd (= low), 50th (= medium) and 66th (= high) percentiles of the temperature range projected for the ECPs. Each line correponds to one of the 81 realizations of the Antarctic Ice Sheet.

TCD
6, 673–714, 2012

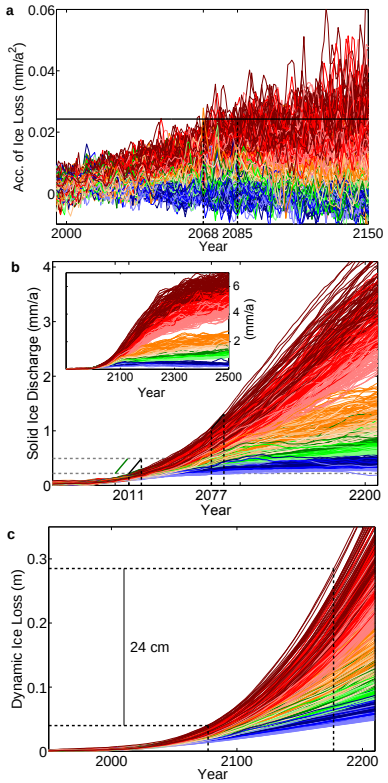

Fig. 18: Panel **a** Acceleration of solid ice loss through warming and precipitation in the ECP-climate scenarios. The black line provides the acceleration of ice discharge as observed by Rignot et al. (2011) of 9 Gt yr^{-2} for the years 1992 to 2009. In our simulations, this value is first reached for the ECP-8.5 scenario between years 2068 and 2085 (see black dashed lines). Panel **b** Associated solid ice discharge. The observed values from Rignot et al. (2011) are displayed in green for the years 2000 to 2009, with the slope of 9 Gt yr^{-2}. The solid ice discharge observed in 2000 is first reached in 2011 in the ECP simulations, but increases more slowly than suggested by the observations (solid black line). For the year 2077 the modelled acceleration concurs with the observed value (see also Panel a). The full timeseries of solid ice discharge is shown in the inlay. Panel **c** Associated ice loss in meters sea-level equivalent. Within the century succeeding 2077, for which the simulated acceleration matches the observed value, the Antarctic ice sheet loses mass equivalent to 0.24 m sea-level rise.

TCD
6, 673–714, 2012

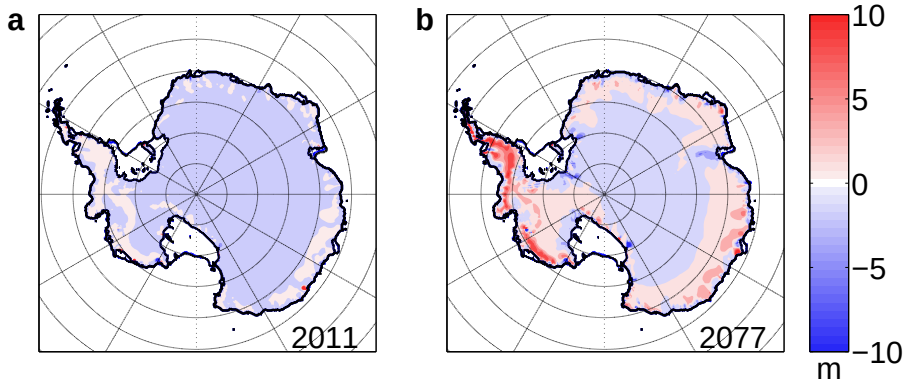

Fig. 19: Ice thickness anomaly to initial state. Shown are the anomalies of those years of the simulation for which the modeled solid ice discharge (Panel a) and acceleration (Panel b) first match the observed values from Rignot et al. (2011), which is in 2011 and 2077, respectively (compare Fig. 18b). The corresponding states of the ice sheet also fulfil the criteria that were applied for selection of the initial ensemble simulations.

TCD
6, 673–714, 2012